Spatial–Spectral Fusion of HY-1C COCTS/CZI Data for Coastal Water Remote Sensing Using Deep Belief Network

Hongren Ji ⓘ, Liqiao Tian ⓘ, Jian Li, Ruqing Tong, Yulong Guo ⓘ, and Qun Zeng

Abstract—The remote sensing monitoring of coastal waters with dramatic changes requires images with high spatial and temporal resolutions and adequate spectral bands. However, a single sensor is limited to meet these requirements. Image fusion is, therefore, widely adopted. In this article, a deep belief network (DBN) is developed to fuse images from the Chinese ocean color and temperature scanner (1000 m, eight bands) and coastal zone imager (50 m, four bands) onboard HaiYang-1C satellite to generate 50-m, eight-band, and three-day observations for coastal waters. The DBN is compared with the existing prevailing Gram–Schmidt transformation (GS) and inversion-based fusion (IBF) algorithms over the Bohai Sea at the top-of-atmosphere reflectance and product [e.g., chlorophyll-a (chl-a)] levels. Results indicate that for the spatial aspect, DBN can avoid the block effect and maintain details. The average structural similarity index of DBN is approximately 22.08% and 3.30% better than that of GS and IBF, respectively; for the spectral aspect, the mean relative errors for eight bands of DBN range from 3.15% to 21.54%. The errors are less than 50% and 80% of those of GS, while less than 80% and 110% of those of IBF, at bands 1–6 and bands 7 and 8, respectively; for chl-a retrieval, DBN yields better results with the coefficient of determination R^2 of 0.78 and root-mean-square error (RMSE) of 0.10 mg/m^3 compared with those of IBF ($R^2 = 0.59$ and RMSE $= 0.16$ mg/m^3). DBN outperforms GS and IBF at reflectance and product levels, displaying great potential for the remote sensing monitoring of coastal waters.

Index Terms—Coastal water, deep belief network (DBN), fusion, HaiYang-1C (HY-1C), remote sensing.

Hongren Ji, Liqiao Tian, and Ruqing Tong are with the State Key Laboratory of Information Engineering in Surveying, Mapping and Remote Sensing, Wuhan University, Wuhan 430079, China (e-mail: jihongren@whu.edu.cn; tianliqiao@whu.edu.cn; tongruqing@whu.edu.cn).

Jian Li is with the School of Remote Sensing and Geomatics Engineering, Nanjing University of Information Science and Technology, Nanjing 210044, China (e-mail: lijian@nuist.edu.cn).

Yulong Guo is with the College of Resources and Environmental Sciences, Henan Agricultural University, Zhengzhou 450002, China, and also with the Henan Engineering Research Center of Land Consolidation and Ecological Restoration, Henan Agricultural University, Zhengzhou 450002, China (e-mail: gyl.zh@henau.edu.cn).

Qun Zeng is with the Editorial Department of Journal, Central China Normal University, Wuhan 430079, China, and also with the School of Urban and Environment Science, Central China Normal University, Wuhan 430079, China (e-mail: zq@mail.ccnu.edu.cn).

I. INTRODUCTION

COASTAL waters are defined as those within close proximity to the land whose water constituents are affected by terrestrial processes [1]. They are important ecological systems and vital assets for many nations, which are also complex and dynamic environments where a vast array of coupled biological, chemical, geological, and physical processes occur over multiple temporal and spatial scales [2]. Coastal areas (within 100 km from the coast) are regions where land, ocean, and atmosphere interact, with approximately 60% of the world's population, and have a direct interface with food supply and human health [3], [4]. Coastal waters are under pressure from direct human activities and climate changes due to their close proximity to the human population [5], [6]. Close to shore and estuaries, coastal water bodies change more rapidly [2]. The remote sensing observations of coastal waters could cover a large area synchronously with a certain periodicity but require remote sensors with high spatial and spectral resolutions.

Satellite remote sensing sensors, however, feature a tradeoff among spatial, temporal, and spectral resolutions [7]. For example, the MODIS onboard Terra/Aqua satellite has 12 spectral bands that are suitable for ocean color remote sensing with wavelengths ranging from the visible (VIS) to the near infrared (NIR) (405–965 nm) and a revisit time of one day, whereas its spatial resolution is 1000 m [8]. The OLI onboard Landsat-8 has a fine spatial resolution of 30 m, but the revisit time is 16 days, which makes applications, such as dynamic coastal monitoring impossible [9]. Its band setting also makes it difficult to retrieve the chlorophyll-a (chl-a) concentration. The panchromatic multispectral sensor onboard Chinese Gaofen-4 is a geostationary sensor, which could provide real-time observations with a spatial resolution of 50 m [10]. Nevertheless, it has only four bands (blue, green, red, and NIR), making it difficult for retrieving several water quality parameters (e.g., chl-a). To alleviate the aforementioned problems, China launched the HaiYang-1C (HY-1C) satellite carrying a high spatial resolution sensor named coastal zone imager (CZI) with a revisit time of three days and an eight-band multispectral sensor named Chinese ocean color and temperature scanner (COCTS) with a revisit time of one day on September 7, 2018 [11]. CZI could meet the spatial requirement with a spatial resolution of 50 m, but it only has four bands (blue, green, red, and NIR). Meanwhile, COCTS has eight typical VIS–NIR bands that are suitable for ocean color remote sensing

but with a spatial resolution of 1000 m. The spatial–spectral fusion of HY-1C COCTS and CZI data could generate 50-m, eight-band, and three-day observations for coastal waters and meet the requirements of spatial and spectral resolutions.

Image fusion has been studied considerably in the remote sensing community. However, most image fusion algorithms are land oriented and the research on ocean color satellite images remains rare. Therefore, fusion algorithms for land targets are often directly applied to water bodies. The conventional image fusion algorithms (pansharpening) include intensity–hue–saturation transformation [12], principal component analysis transformation [13], [14], Brovey transformation [15], wavelet transformation [16], Gram–Schmidt transformation (GS) [17], and so on. Du *et al.* [18] proved that GS performs the best for water bodies in the above-mentioned algorithms. The greatest problem for the conventional image fusion algorithms is that they are designed for panchromatic and multispectral image fusion and only one panchromatic image for multispectral images can be received [19], that is, the image fusion between two multispectral sensors (e.g., four-band CZI and eight-band COCTS) could only have one band from CZI images for the fusion of COCTS data, leading to a considerable loss of spatial information in CZI images. In addition, several image fusion algorithms have been applied in the ocean color remote sensing. Ashraf *et al.* [20] tested the subtractive resolution merging technique, which uses a mix of both spatial and spectral centric approaches, under a semiaquatic freshwater environment in New Zealand. For coastal waters, Minghelli-Roman *et al.* [21] improved MERIS resolution by merging its images with Landsat-7 ETM+ images by implementing unmixing-based multisensory multiresolution fusion [22]. For inland waters, Guo *et al.* [23] proposed an inversion-based fusion (IBF) algorithm that performed better than the unmixing-based fusion algorithm.

The key issue for data fusion is how to build the relationships among various data, which is exactly what deep learning is good at [24]. Deep learning can capture the abstract features of remote sensing observations and learn the potential associations among different observations through multilayer learning [7]. The four mainstream deep learning architectures are the autoencoder, convolutional neural network (CNN), recurrent neural network, and deep belief network (DBN). With the autoencoder, Liu *et al.* [25] proposed a band-independent encoder–decoder network for pansharpening of remote sensing images. With the CNN, the most commonly used deep learning architecture in remote sensing, different research articles have been carried out, such as cross-source image retrieval [26], deep representation of images [27], scene image super resolution [28], [29], and image fusion [30]–[32]. With the DBN, another widely applied deep learning architecture in remote sensing, the classification of hyperspectral images [33]–[35], hyperspectral image representation [36], object detection [37], and various other research articles have been done, whose results demonstrated the accuracy and efficiency of the DBN model. In 2018, Shen *et al.* [38] applied DBN to the prediction of ground-level PM2.5 by using the top-of-atmosphere (TOA) reflectance of MODIS, indicating that the DBN has potential in predicting continuous data, such as fusion data. Combined with large amounts of training data, the DBN
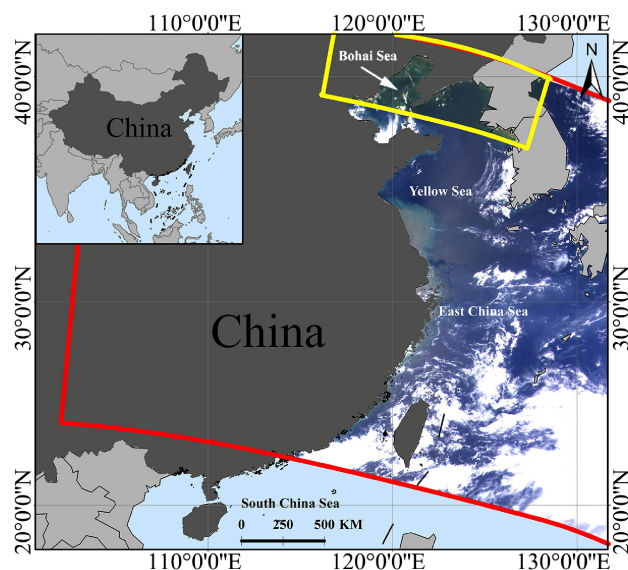

Fig. 1.   Location of the Bohai Sea. The edge of an HY-1C COCTS image is in red and the edge of an HY-1C CZI image is in yellow.

is expected to build the accurate spatial–spectral fusion model and improve the quality of fusion images.

In this article, a DBN model is built to fuse HY-1C COCTS and CZI images and generate 50-m, eight-band, and three-day observations for coastal waters. The model is tested on the Bohai Sea and compared with GS and IBF algorithms at TOA reflectance and product (chl-a concentration in this study) levels. Specifically, the training dataset is from one pair of COCTS and CZI images on August 16, 2019, and the validation dataset consists of 13 pairs of COCTS and CZI images from August 19, 2019 to November 22, 2019. The DBN-fused TOA reflectance and chl-a concentration are compared with those from GS, IBF, and official standard products to evaluate the performance of the DBN model.

II. MATERIALS AND METHODS

A. Study Area and Dataset

1) Study Area: The Bohai Sea (37°07′–41°N, 117°35′–122°15′E, as shown in Fig. 1) is a semienclosed marginal sea in the northwestern Pacific Ocean on the northern coast of China. It has a water area of ∼77 000 km^2, a water volume of 1700 km^3, and an average depth of 18 m [39]. The motion of water masses is dominated by semidiurnal and diurnal tides, which account for approximately 60% of the current variation and kinetic energy there [40]. Connected with the Yellow River, the second-longest river in China, the Bohai Sea receives 1.10×10^9 tons of sediment per year [41]. The environment of the Bohai Sea has been deteriorated by contaminants dumped into the sea [39] and the intensity of coastal land use has become increasingly high with the rapid economic development. Several problems, such as destroyed and occupied coastal wetland, estuarine pollution, eutrophication of seawater, and occurrence of red tide, occur frequently, which affect the sustainable development of the region [42]. In the past several decades, the Bohai Sea has become

TABLE I
DATE AND TEMPORAL GAP OF HY-1C COCTS/CZI IMAGES

	Date (temporal gap)		
training	0816 (00)		
validation	0819 (03)	0825 (09)	0828 (12)
	0831 (15)	0903 (18)	0915 (30)
	0918 (33)	0921 (36)	0927 (42)
	0930 (45)	1015 (60)	1105 (81)
	1122 (98)		

Note: Date is in the format of MMDD, and temporal gap is in the unit of day.

highly productive but polluted with green macroalgae blooms reported in recent years [43]. Approximately 0.18 million water transport vessels [44] and 1.07 million fishing boats [45] were in operation over the Chinese seas by 2013, approximately one-third of which navigated over the Bohai Sea [46]. The ecosystem of the Bohai Sea is rapidly degrading and the sea has basically lost its ecological function [47]. Thus, the high spatial–spectral resolution remote sensing observations of the water quality of the Bohai Sea are crucial for government decision making.

2) Dataset: In this study, 14 pairs of HY-1C COCTS and CZI images are obtained from the National Satellite Ocean Application Service of China (NSOAS),[1] for DBN training and validation. The training dataset contains one pair of COCTS and CZI images of the Bohai Sea on August 16, 2019. The validation dataset has 13 pairs of COCTS and CZI images from August 19, 2019 to November 22, 2019. The maximum temporal gap is 98 days. In addition, the geostationary ocean color imager (GOCI) standard chl-a product of August 28, 2019 is acquired for the validation of fused retrievals of chl-a. The details are listed in Table I.

HY-1C COCTS and CZI have complementary settings. The COCTS has 2900 km swath width, 1-km spatial resolution, and eight VIS–NIR bands. The central wavelengths of COCTS bands are 412, 443, 490, 520, 565, 670, 750, and 865 nm. The CZI has a 950 km swath width, 50 m spatial resolution, and four VIS–NIR bands. The central wavelengths of CZI bands are 460, 560, 650, and 825 nm. The spectral bands of COCTS and CZI are plotted in Fig. 2. COCTS and CZI have a short revisit time (no more than three days). COCTS and CZI sensors are jointly carried on HY-1C satellite; hence, the fusion of COCTS and CZI images has the advantages of a short time interval, consistent observation attitude, and high similarity of atmospheric conditions, compared with the image fusion of other sensors.

GOCI provides chl-a concentration products in near real time during the daytime, from 09:16 to 16:16 local time (a total of eight images per day), with a spatial resolution of 500 m [48]–[50]. The GOCI-derived ocean color data can provide an effective tool to monitor ocean phenomena in the region, such as the diurnal variation of ocean optical and biogeochemical properties [51]. A significant noise reduction is found in the chl-a product at low concentrations (<0.25 mg/m^3), leading to a high precision ($\sim$3% uncertainty) [52]. Thus, GOCI chl-a concentration products are suitable for the validation of DBN-fused
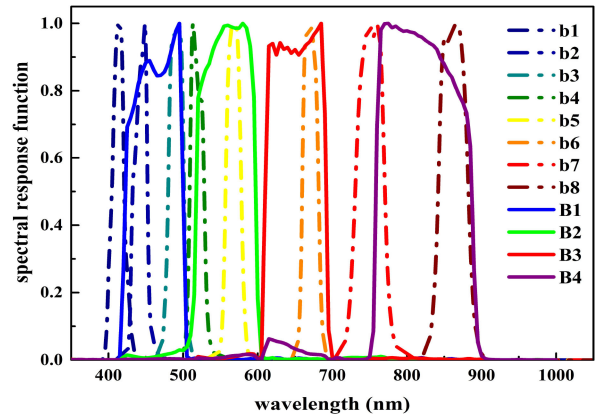

Fig. 2. HY-1C COCTS/CZI spectral response function. The small letters represent COCTS bands (dash–dotted line), and the capital letters represent CZI bands (solid line).

chl-a retrievals. The product is available at the official website of Korea Ocean Satellite Center.[2]

B. Methods

1) Preprocessing of HY-1C COCTS/CZI Image: The original pixel value is a digital number DN and is converted into a radiance value through radiometric calibration (1). The calibration parameters (gain and offset) are provided by the metadata of each image

$$L_{\text{TOA}} = \text{gain} \cdot \text{DN} + \text{offset} \tag{1}$$

where L_{TOA} is the radiance of TOA.

The image radiance is related to environmental factors and imaging geometry (e.g., solar–terrestrial distance, solar irradiance, and solar zenith angle); therefore, the radiance is further converted to the reflectance through (2) [53]. The reflectance is the percentage of radiant energy reflected by an object in the total radiant energy, which is mainly determined by the nature of the material itself [54]. It reduces the cosine effect of different solar zenith angles due to the time differences among data acquisitions. It also compensates for the different values of solar irradiance arising from spectral band differences

$$R_{\text{TOA}}(\lambda) = \pi \cdot L_{\text{TOA}}(\lambda) \cdot d^2 / (E_0(\lambda) \cdot \cos\vartheta_s) \tag{2}$$

where d represents the earth–sun distance in astronomical units, $E_0(\lambda)$ is the extraterrestrial solar irradiance, and the pixel-specific sun zenith angle is denoted as ϑ_s. $E_0(\lambda)$ is calculated as follows [55]:

$$E_0(\lambda) = \int L_{\text{TOA}}(\lambda) \cdot \text{RSR}(\lambda) \, d\lambda / \int \text{RSR}(\lambda) \, d\lambda \tag{3}$$

where $\text{RSR}(\lambda)$ is the spectral response function of the corresponding band.

2) Establishment of the DBN Model: The key point of the DBN algorithm is how to acquire the mapping relation from CZI bands to COCTS bands. Once the mapping relation is known, four-band CZI images could be extended to eight-band ones

[1][Online]. Available: https://osdds.nsoas.org.cn/#/

[2][Online]. Available: http://kosc.kiost.ac.kr/eng/p10/kosc_p11.html

reliably. To ensure high accuracy, the following three premises are necessary.

1) A correlation exists between the adjacent wavelengths.
2) The spectral mapping of the same region is relatively stable.
3) The more consistent the band coverage is, the more accurate the prediction is.

Generally, the mapping from hyperspectral bands to a multispectral band is as follows:

$$y_1 = a_{11}x_1 + a_{21}x_2 + \ldots + a_{n1}x_n$$
$$y_2 = a_{12}x_1 + a_{22}x_2 + \ldots + a_{n2}x_n$$
$$\vdots$$
$$y_m = a_{1m}x_1 + a_{2m}x_2 + \ldots + a_{nm}x_n \qquad (4)$$

where y is the value of the multispectral band, a is the weight of the hyperspectral band according to the spectral response function, and x is the value of the hyperspectral band. If we have hyperspectral values, we can calculate unique multispectral values under the condition that the spectral response function is known. Nonetheless, the values are uncertain if we perform the opposite process. The number of equations is smaller than that of the unknown quantities ($m < n$); thus, we need $n - m$ points at least. However, the observed value differs from the calculated value when considering the actual situation, in accordance with the following equation:

$$x_{\text{obs}} = \alpha\hat{x} + \Delta x_1 + \Delta x_2 \qquad (5)$$

where x_{obs} is the observed value, α is the scale factor, $\hat{x}$ is the true value, Δx_1 is the systematic error, and Δx_2 is the accidental error.

To reconstruct eight COCTS bands from four CZI bands, we need to construct at least $4n\text{-}m$ ($4 \times 8 - 4 = 28$) equations. The more equations we have, the less accidental error remains. Learning through a large amount of data, DBN could gain robust relations among COCTS and CZI bands, construct the equations, and obtain optimizations and solutions. The fused eight-band CZI values are then calculated.

The DBN in this study consists of one input layer, two hidden layers, and one output layer. The TOA reflectance of CZI is selected as the input data. The structure of DBN is shown in Fig. 3 and explained as follows.

1) Input layer: TOA reflectance of four CZI bands.
2) Hidden layer: Two fully connected hidden layers with 64 nodes of each layer, and ReLU is chosen as the activation function.
3) Output layer: TOA reflectance of eight COCTS bands.

A general DBN structure is used in this research [7], [38]. ReLU, the most widely used activation function, is chosen. The number of nodes of each layer is selected as the multiple of band numbers (4 and 8) since the number of decomposed values from bands is the multiple of band numbers. Several multiples of band numbers are tested preliminarily, such as 16×16, 32×32, 64×64, 128×128, 256×256, and 512×512. For the combinations 1 and 2, the precision is low; for the combinations 4–6, the precision shows no obvious improvement but more training
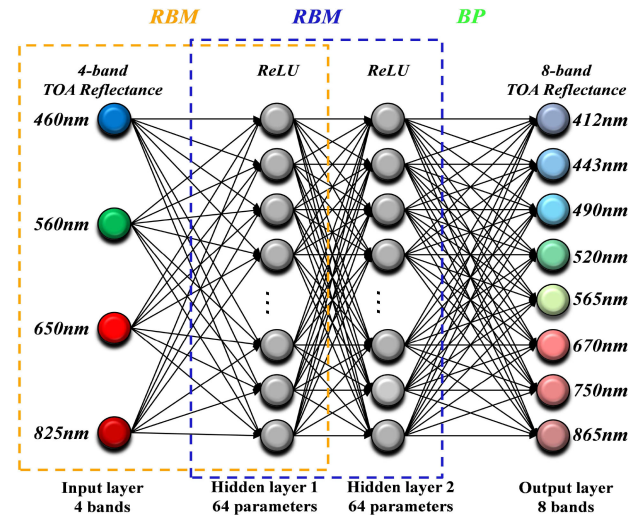

Fig. 3. Structure of DBN. Training: The input four-band and eight-band data are the spatially resampled CZI TOA reflectances and original COCTS TOA reflectances, respectively. Validation and application: The input four-band and output eight-band data are the original CZI TOA reflectances and TOA reflectances of the fused image with similar bands of COCTS and the spatial resolution of CZI, respectively. More details are further elaborated in Section IV-C.
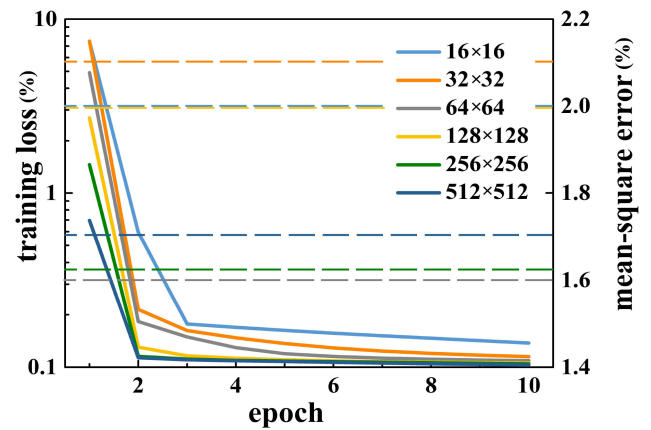

Fig. 4. Training losses of hidden layers with different nodes (solid lines). MSEs calculated from another image pair (dash lines). The training loss axis is logarithmic. The legend describes the numbers of nodes in the two hidden layers. For example, "16×16" means that the two hidden layers have 16 nodes and 16 nodes, respectively.

space and data are acquired. The validation shows that the 64×64 structure maintains the lowest mean-square error (MSE) when they are examined by another image pair (see Fig. 4).

DBN is first pretrained using the input data and restricted Boltzmann machine to generate the initial model coefficients without supervision. This step can avoid the local optimum and long training time that the traditional neural networks (such as the backpropagation neural network) have because the weighted parameters are not randomly initialized. Then, the MSE between the DBN prediction and reference data is calculated for the backpropagation algorithm [56]. The circulation breaks when MSE shows no distinct decrease within ten epochs to avoid overfitting.

3) Performance Evaluation: The prevailing fusion methods of GS and IBF are selected to evaluate the effectiveness of DBN. We select five indices, namely, the coefficient of determination R^2, root-mean-square error (RMSE), relative error (RE), structural similarity index (SSIM), and goodness-of-fit coefficient (GFC), to evaluate the accuracy of fusion images. SSIM is an indicator of the spatial structure preservation of the estimated image. The higher the SSIM is, the better the spatial structure preservation will be [57], [58]. GFC is used to verify the quantitative performance of the spectral reflectance reconstruction. It measures the similarity between the actual and reconstructed spectral reflectance [59]. The formulas for SSIM and GFC are as follows:

$$\text{SSIM}\,(\rho, \hat{\rho}) = \frac{1}{S} \sum_{i=1}^{S} \text{SSIM}\left(\rho^i, \hat{\rho}^i\right) \tag{6}$$

$$\text{GFC} = \frac{1}{N} \frac{\left|\sum_\lambda \rho\,(\lambda)\,\hat{\rho}\,(\lambda)\right|}{\sqrt{\sum_\lambda \left[\rho\,(\lambda)\right]^2}\sqrt{\sum_\lambda \left[\hat{\rho}\,(\lambda)\right]^2}} \tag{7}$$

where $\text{SSIM}(\rho^i, \hat{\rho}^i)$ is the SSIM computed between the "true" and estimated band ρ^i and $\hat{\rho}^i$, and S is the number of bands. $\rho(\lambda)$ and $\hat{\rho}(\lambda)$ are the "true" and estimated spectral reflectance, and N is the number of pixels in the image, respectively. Note that only the final step of the SSIM calculation is shown because the whole formula is complicated but not all necessary [57]. The formula and its derivation process could be found in [58].

III. RESULTS

A. Spatial Performance of Fused Reflectance

1) Visual Examination of True Color Images: The RGB fusion results of GS, IBF, and DBN are shown in Fig. 5, and RGB COCTS and CZI images are also plotted for direct visual evaluation at spatial and spectral aspects. In the first column of Fig. 5, the true color synthetic images of COCTS, GS fusion, IBF fusion, DBN fusion, and CZI show similar color distributions. In the second column of Fig. 5, COCTS is excessively coarse to determine the ship wake, the fused images and CZI image are able to observe the small ship, and the image color of the DBN fusion is the closest to that of COCTS. In the third column of Fig. 5, the water frontal surface is clearer and sharper in Fig. 5(i) (IBF fusion) and Fig. 5(l) (DBN fusion) than that in Fig. 5(f) (GS fusion). This finding suggests that the three fusion algorithms can improve the spatial resolution, whereas DBN can maintain most spectral information. In the third column of Fig. 5, the clouds are within the scenes. COCTS and GS-fused images display a color deviation at the cloud edge, whereas IBF- and DBN-fused images can avoid this effect and obtain clear images comparable with the CZI image. From the direct visual examination, we can determine the following.

1) GS, IBF, and DBN can improve the spatial resolution of COCTS without changing the color distributions.
2) DBN outperforms GS and IBF regarding spectral information preservation.
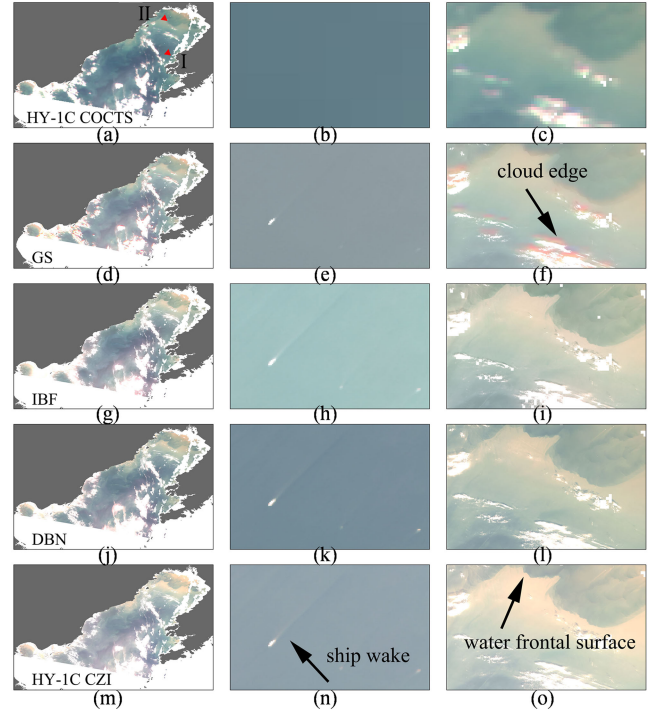3) GS has problems in fusing the pixels at cloud edges.

Fig. 5. (a)–(c) RGB images of HY-1C COCTS. (d)–(f) GS fusion. (g)–(i) IBF fusion. (j)–(l) DBN fusion. (m)–(o) HY-1C CZI. Images in the second (ship) and third (cloud) columns are the regional expansion of images in the first column at I and II, respectively.

2) Spatial Distributions of REs and Regression Analysis: The REs of the entire fusion image acquired on August 16, 2019 are calculated and shown in Fig. 6 with the COCTS image as a reference. For the GS-fused image, the REs are significantly higher than those of the IBF- and DBN-fused images. The REs of most regions are higher than 20% and that of approximately one-third of the region are approximately 40% at bands 7 and 8. In Fig. 6(f)–(h), high REs appear in the image center. They basically coincide with much clearer water with a much lower reflectance signal in red–NIR bands. Thus, there is a great possibility that the high REs are caused by the decrease in the denominator and lower signal–noise ratio (SNR) at longer bands. For the IBF-fused image, the REs are similar to those of the DBN-fused image, indicating that the performance of DBN is comparable with that of IBF and better than that of GS in terms of REs in comparison with the COCTS image. For the DBN-fused image, REs are less than 10% in most areas of the Bohai Sea at bands 1–6, whereas they may reach approximately 40% in some areas at bands 7 and 8. This difference may be caused by the fact that for longer bands, the reflectance is far less than that of the shorter bands due to strong water absorption. The decrease in denominator results in the overall increase in REs. Moreover, the lower SNR at longer bands may lead to larger REs.

The regression analysis of TOA reflectance between the fused images and the reference image (COCTS image) is conducted and plotted in Fig. 7 to assess the reflectance of fused images quantitatively. The performance of the GS algorithm is the poorest among the three fusion methods with the largest RMSE
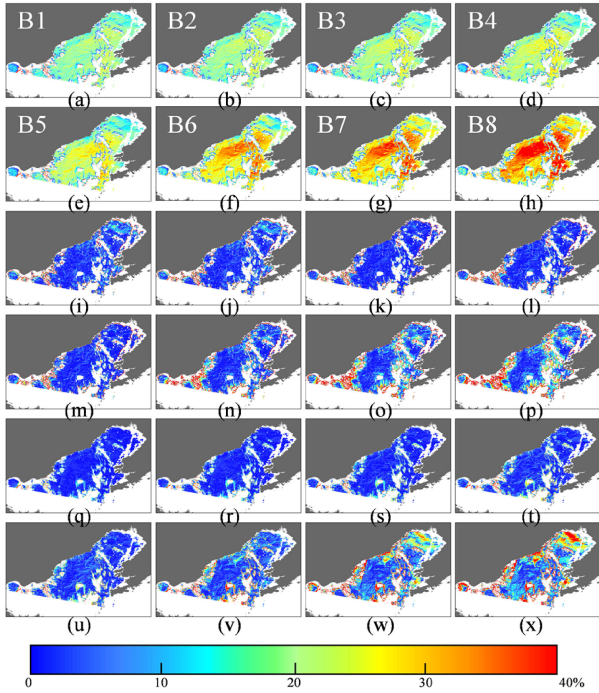
Fig. 6. RE maps of (a)–(h) GS-, (i)–(p) IBF-, and (q)–(x) DBN-fused images at bands 1–8 (*B*1–*B*8). Note that the COCTS image is used as a "true" value.
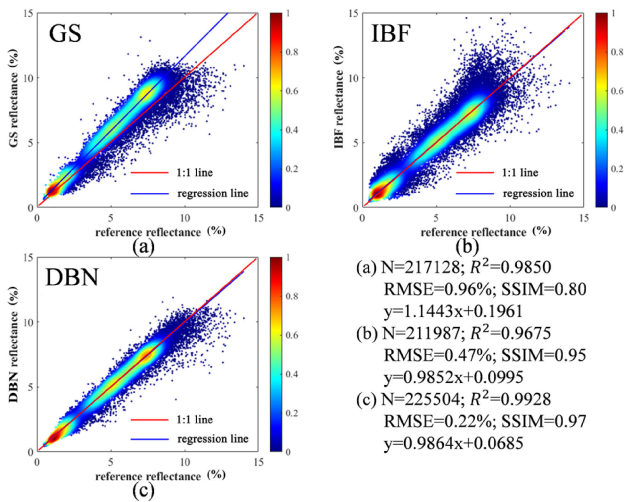

Fig. 7. Regression analysis of (a) GS-, (b) IBF-, and (c) DBN-fused images with the reference COCTS image.

of 0.96% and the smallest SSIM of 0.80. Although the R^2 is larger than 0.98, the gain coefficient of the fitting line is far away from 1:1, suggesting that GS may overestimate the reflectance during the fusion.

The IBF algorithm has the smallest R^2 among the three algorithms, indicating that the prediction of IBF contains the most uncertainties. Consequently, the scatters of the IBF algorithm are substantially diffuse. In Fig. 7(b), a small number of scatters away from the fitting line are the hot pixels, which are produced by wrong pixel matching and excessive prediction errors. The reflectance of DBN-fused and COCTS images is
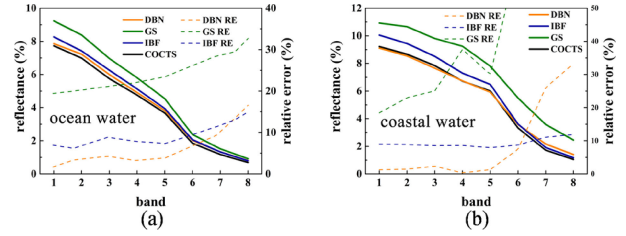

Fig. 8. COCTS and fused spectra (solid lines). REs are in dash lines. (a) Ocean water. (b) Coastal water.

closely distributed to 1:1 line with the highest R^2 of 0.9928, SSIM of 0.97, and the smallest RMSE of 0.22%, indicating that the DBN algorithm can make stable and reliable predictions. The regression analysis demonstrates that DBN is the best fusion algorithm among the three methods.

B. Spectral Performance of Fused Reflectance

1) Spectral Consistency: The relative relationship among bands, that is, the shape of the spectral curve, is a piece of important information contained in remote sensing images. We randomly select an ocean water pixel and a coastal water pixel from fused images to compare their spectra with the "true" spectra of COCTS. The results are shown in Fig. 8.

For the ocean water pixel, the prediction errors of GS are larger than 20% for all bands, although the spectral shape is correct. The prediction errors of IBF are within 20% but approximately 5% higher than those of DBN. The spectrum of the DBN-fused image is highly consistent with that of the COCTS image. The prediction errors are within 10% for bands 1–6 and within 20% for bands 7 and 8.

For the coastal water pixel, the prediction of GS is always higher than "true" values. And GS performs the worst among the three algorithms. As for IBF, it could maintain the prediction errors of approximately 10% for all bands. For bands 7 and 8, it performs better than DBN, although its prediction errors also increase. The prediction errors of DBN are within 5% for bands 1–5. For bands 6–8, a significant increase in prediction errors occurs. The reason is that NIR bands have a relatively low SNR compared with VIS bands.

To sum up, DBN performs best at bands 1–6, IBF is the best fusion algorithm at bands 7 and 8, and GS has the worst performance and overestimates the reflectance values.

2) Spectral Mean RE: The mean REs (MREs) of each band from GS, IBF, and DBN compared with COCTS are shown in Fig. 9. The MREs of DBN are obviously smaller than those of GS. Specifically, the DBN MREs of bands 1–8 are 82%, 79%, 76%, 69%, 68%, 53%, 32%, and 23% less than those of GS, respectively. Compared with the MREs of IBF, the MREs of DBN are smaller at the first six bands and are 72%, 67%, 55%, 45%, 41%, and 22% smaller, respectively. Nonetheless, IBF performs better at bands 7 and 8, and the MREs of DBN are 0.2% and 9% larger, respectively.

The lower fusion accuracy at bands 7 and 8 is related to the lower SNR. COCTS and CZI sensors have a relatively low SNR
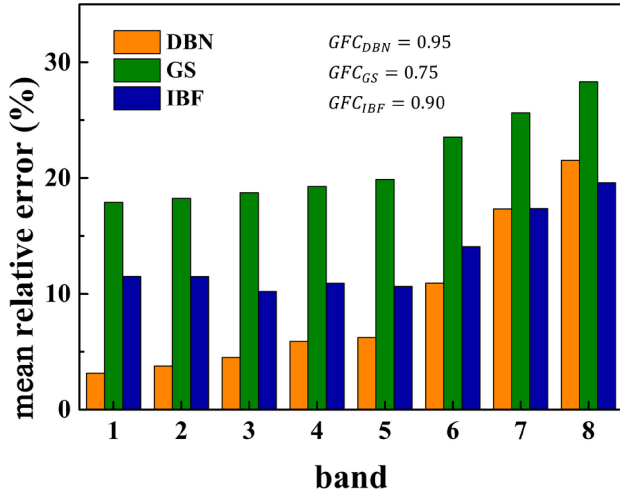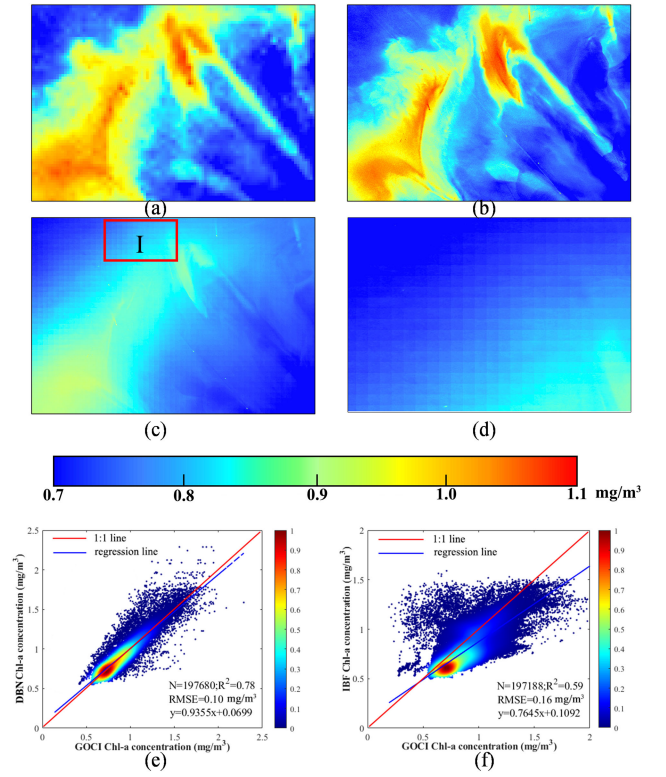
Fig. 9. MREs of DBN, GS, and IBF algorithms.

Fig. 10. (a) GOCI chl-a product. (b) Chl-a derived using a DBN-fused image. (c) Chl-a derived using an IBF-fused image. (d) Regional expansion of Fig. 10(c) at I. (e) Regression analysis between GOCI and DBN chl-a products. (f) Regression analysis between GOCI and IBF chl-a products.

in the NIR bands, which results in considerable uncertainties. Fig. 9 shows that the MREs of the three algorithms are higher at NIR bands 7 and 8. GS and IBF use the corresponding COCTS pixels as guidance; as a result, MREs are constrained. However, DBN reconstructs spectra in accordance with CZI pixels without COCTS pixels; thus, poor data quality could cause greater errors for DBN.

GFCs are also calculated and plotted in Fig. 9. GFC indicates improved performance when it is close to 1. The GFC of GS is much smaller than those of IBF and DBN. Although both the GFCs of IBF and DBN are high and larger than 0.9, the GFC of DBN is the highest and reaches 0.95, indicating that DBN can best preserve spectral shape.

C. Performance of Chl-a Retrieval

Chl-a is one of the three most frequently retrieved water parameters by remote sensing [60]. The RGB + NIR four-band setting of the CZI sensor makes it difficult to conduct accurate retrieval because of the lack of chl-a sensitive bands [61]. We have obtained an eight-band-fused image; its capability in the chl-a retrieval should be evaluated. According to NSOAS [11], bands 2, 3, and 5 of COCTS are highly sensitive to the chl-a concentration. As shown in Fig. 9, the MRE of DBN at the three bands is the smallest among the three algorithms, indicating that the DBN-fused image may perform the best in the chl-a retrieval.

In this study, the GOCI standard chl-a product is used as the "true" value, which has been widely proven accurate [50]–[52], [62]. The chl-a concentration of fused images is retrieved as follows [63]:

$$CHL = 1.853 \left(\frac{B1 + B2 - B3}{B4} \right)^{-3.263} \quad (8)$$

where $B1$, $B2$, $B3$, and $B4$ are the atmospherically corrected reflectance by using the revised Rrs (NIR) model [64] of the second, third, first, and fifth band of the fused images, respectively.

The GS algorithm is not adopted here because it has been proven obviously inferior to DBN and IBF. The GOCI standard chl-a product and chl-a derived from DBN- and IBF-fused images are shown in Fig. 10. The DBN-derived result of chl-a, as shown in Fig. 10(b), achieves higher precision at both low and high concentrations than the IBF-derived result, as shown in Fig. 10(c). The spatial distribution of DBN-derived chl-a shows more obvious gradations. It proves that the DBN algorithm improved the spatial resolution and maintained the details. However, the IBF algorithm improves the spatial resolution but loses more crucial details than the DBN-derived result. The regression analysis between them is also plotted. The regression results prove that the pixels of the IBF-fused image are more dispersed with an R^2 of 0.59 and RMSE of 0.16 mg/m^3. The gain factor of the fitting line is 0.76, which is far away from 1:1 line, indicating that the chl-a concentration retrieved from the IBF-fused image is generally underestimated. In addition, from Fig. 10(d), the enlargement of Fig. 10(c), the IBF algorithm leads to the block effect. The block effect makes the fused image homogeneous and smooth, but adjacent fused pixels are anomalously different at block edges.

Benefited from reconstructing spectra pixel-by-pixel, the DBN algorithm is free from the block effect. With the highly accurate spectra and 50-m spatial resolution, the retrieved chl-a concentration from the DBN-fused image is well consistent with that of the GOCI standard product with improved spatial
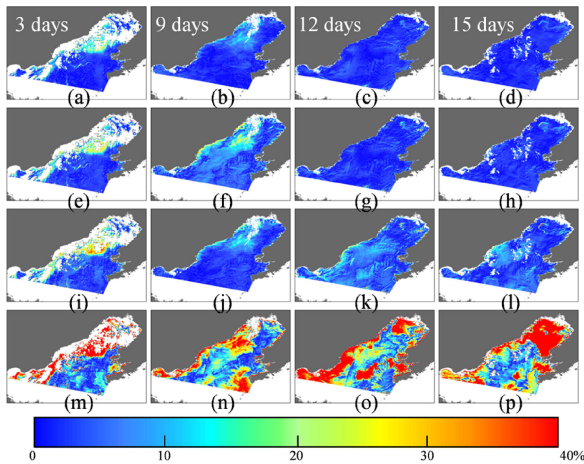
Fig. 11. RE distribution of different bands and days of DBN images. Rows 1–4 are the RE spatial distribution of different bands. (a)–(d) Band 2. (e)–(h) Band 3. (i)–(l) Band 5. (m)–(p) Band 8. Columns 1–4 are the fusion images on different dates. (a), (e), (i), and (m) August 19, 2019. (b), (f), (j), and (n) August 25, 2019. (c), (g), (k), and (o) August 28, 2019. (d), (h), (l), and (p) August 31, 2019. The DBN model is trained using the COCTS and CZI image pair on August 16, 2019.
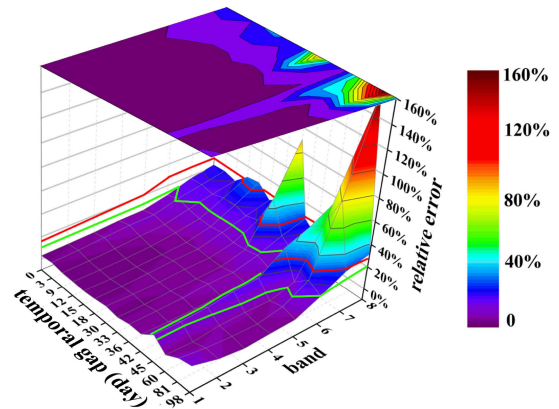

Fig. 12. Variations in the RE of the DBN-fused image along with temporal gaps. The RE surface below the red (GS) or green (IBF) line indicates that the DBN has better performance than GS or IBF modeled and applied on the same day.

resolution and more details. As a result, DBN achieves a higher R^2 of 0.78 and a lower RMSE of 0.10 mg/m^3 than IBF.

IV. DISCUSSION

A. Influence of Temporal Gaps Between Image Pairs

Ideally, fusion results with the highest accuracy can be obtained through modeling and applying by using intraday images. However, the reality is that the optical remote sensing images are often covered by clouds, resulting in the lack of fusion image pair on the same day. Therefore, exploring how the temporal gap between the training and applying data influences the COCTS and CZI mapping relationship is necessary.

Specifically, we first use an image pair acquired on August 16, 2019 to build the DBN model and apply this model to the CZI images acquired on August 19, 25, 28, and 31, 2019. The spatial distribution of RE on different dates is shown in Fig. 11. The REs at bands 2, 3, and 5 are relatively low, regardless of the temporal gaps. Nevertheless, at band 8, the RE increases as the temporal gap increases. The RE increases gradually from band 2 to 8, which could be attributed to the lower SNR at longer COCTS bands. The SNRs of COCTS bands 2, 3, 5, and 8 are 767, 668, 637, and 424, respectively.

The cloud edge pixels of DBN have high RE, especially on August 19 and 25, 2019, because the thin clouds around thick clouds are difficult to discriminate. The COCTS and CZI sensors record the mixed spectra of clouds and water for thin clouds. Compared with pure water spectra, the mixed spectra contain more uncertainty from thin cloud pixels.

Thus, the temporal gaps of the training and applying data of DBN should be carefully selected. For VIS bands, the temporal gap can be relatively long; for inhomogeneous areas, the temporal gap should be shorter than that for homogeneous regions.

In consideration of the number of available images and the temporal influence, a temporal gap of 98 days (about three months) is selected. During this period, 14 images are available, which are enough for training and validation. Fig. 12 shows that with an increase in the temporal gap, RE is undoubtedly increased, but the growth rate is low. The unusual RE of the fused image with a 33-day or 81-day temporal gap is mainly caused by the thin cloud covering almost the entire image. In most cases, the RE of the DBN-fused image at bands 1–6 is lower than that of the IBF-fused images. When the temporal gap is within 30 days, the RE of the DBN-fused image at bands 7 and 8 is higher than that of the IBF-fused images. This is consistent with the above-mentioned conclusion. When the temporal gap is up to 30 days, the RE at band 8 increases to the level of the GS algorithm. When the temporal gap is up to 98 days, the RE of VIS bands 1–5 is still lower than 20%. Therefore, images before and after the target time can be used for training, and images with the temporal gaps of more than 30 days are not recommended.

Considering that the revisit time of HY-1C is approximately three days, we can acquire several images of the target regions every month, which will greatly increase the possibility of obtaining adequate image pairs. Despite pixels with good qualities on the same day are insufficient, adjacent image pairs on other days can be used to train the DBN model because of the high-frequency HY-1C observations.

B. Fusion at the Reflectance or Product Level

In this study, we fuse images from HY-1C COCTS and CZI, which are designed for the ocean color remote sensing and water quality monitoring. Thus, the retrieval of water quality parameters (e.g., chl-a) is the primary goal of HY-1C, and we try to understand whether we should fuse COCTS and CZI at the reflectance or product level.

The GOCI chl-a product is used to fuse the COCTS-derived chl-a product, considering that CZI is unsuitable to derive the chl-a concentration directly. The GOCI chl-a product is also used as the "true" value, which may give advantages to this
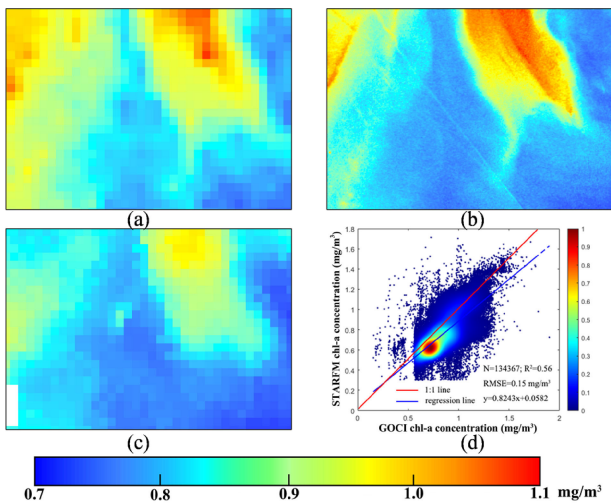
Fig. 13. (a) GOCI standard chl-a product (500 m). (b) Retrieved chl-a concentration by using the DBN-fused image (50 m). (c) Fused chl-a concentration by using the STARFM algorithm (500 m). (d) Regression between the GOCI standard chl-a product and the fused chl-a concentration by using the STARFM algorithm.

fusion. The widely used STARFM algorithm without additional bands needed is adopted to complete the fusion at the chl-a level. The STARFM algorithm has been successfully used for the fusion of water parameters [65]–[67]. The GOCI standard chl-a product, DBN-fused chl-a map at the reflectance level, and STARFM-fused chl-a product at the chl-a level are shown in Fig. 13.

Restricted by the 500 m GOCI standard chl-a product, the STARFM-fused chl-a image could not reveal fine details, such as the disturbance of the ship wake in the DBN-fused chl-a map. In addition, the high value of the STARFM-fused chl-a image is obviously lower than the "true" value, indicating that STARFM tends to underestimate chl-a values, as proven by the gain factor ($0.82 < 1.0$) of the fitting line in Fig. 13(d). The gain factor of STARFM at the chl-a level (0.82) is worse than that of DBN at the reflectance level [0.93, as shown in Fig. 10(e)], and the R^2 (0.56) is also much lower than that of the DBN-fused chl-a concentration [0.78, as shown in Fig. 10(e)].

Although using the GOCI chl-a product as the "true" value provides privileges to fusion at the chl-a level, its performance is still worse than that of the DBN-fused image at the reflectance level. Thus, fusing images at the reflectance level rather than at the product level is recommended because the spectral information will not be lost. CZI is also unsuitable to derive several water quality parameters (e.g., chl-a) due to the lack of spectral bands.

C. Comparison Among GS, IBF, and DBN Algorithms

The procedure of the GS algorithm is described as follows.
1) A low spatial resolution panchromatic band simulated using the multispectral bands is added, and GS is applied.

2) The input high spatial resolution panchromatic band is adjusted to be consistent with the low spatial resolution panchromatic band after GS.
3) The high spatial resolution panchromatic band is used to replace the low spatial resolution panchromatic band, and inversed GS is used to add spatial information [17].

The inevitability of imaging gaps reveals the natural defects of the GS fusion: first, differences between the two images caused by temporal gaps will cause serious errors to the fusion results, which cannot be predicted or avoided; second, the accurate registration is extremely difficult under the condition that the spatial resolution of CZI is $20\times$ higher than that of COCTS, which means one COCTS pixel corresponds to 400 CZI pixels. Therefore, the incorrect correspondence of edge pixels is common in all image pairs.

The procedure of the IBF algorithm is as follows.
1) The spectral and spatial resolutions are enhanced via normalization and bilinear interpolation.
2) The ratio matrix, which is defined as the ratio of each pixel in an $n \times n$ region, is calculated.
3) Seed pixel spectra, the independent variables in the inversion system, are retrieved, and least squares inversion is performed via the minimization of the cost function by using the quasi-Newton method.
4) The spectra of other pixels in the region are calculated, and this step is repeated until all regions are processed [23].

The IBF fusion process is guided by COCTS images. The value of the fused spectrum is restricted by that of the COCTS spectrum. As a result, the MREs of all bands are close. The block effect of IBF is caused by its principle and a 20×20 window exists for each COCTS pixel. This finding suggests that spectra at the window edge are relatively different from those of the adjacent pixels corresponding to another window.

The DBN model is first trained using the resampled CZI images and concurrent COCTS images and learns spectral mapping relationships between the CZI and COCTS bands. Then, the values of fused images are recovered pixel-by-pixel based on nonresampled CZI images. In the first step, COCTS and CZI images are matched according to their spatial information. Specifically, CZI images are resampled to the spatial resolution of COCTS images after the image registration. Using COCTS images as the "true" values, the DBN model learns the mapping relationships between the input CZI and COCTS bands. The high-resolution spatial information of CZI is lost at this stage, while the spectral mapping relations are learned. In the second step, when the DBN model is applied to other CZI images, the CZI images remained nonresampled to maintain the high-resolution spatial information and learn spectral information of COCTS from DBN. Thus, the fused images are with the spectral information of COCTS and the spatial resolution of CZI. The aforementioned problems are avoided in principle. If the two mapping images have differences caused by the temporal gap, the ground objects in the DBN-fused image will be the same as those in the CZI image because only the CZI image is used in the spectral reconstruction. The effect of registration deviation can be corrected using the majority of normally corresponded pixels in DBN learning and training because incorrectly corresponded

pixels only account for a small proportion and their influence on the final weights is negligible. Without the guidance of COCTS images, the inconsistency caused by lower SNR at longer bands could contribute to much more errors for the DBN method than the IBF method. This is why DBN performs better in bands 1–6 rather than bands 7 and 8.

As a result, compared with GS and IBF algorithms, DBN alleviates the problems of color deviation, spectral distortion, and block effect. The DBN-fused images perform well at the reflectance level and chl-a retrieval level. It is the best fusion method among the three algorithms and is suitable to fuse COCTS and CZI images for the remote sensing of coastal waters.

V. CONCLUSION

Monitoring the details of water bodies is of great significance. COCTS and CZI onboard HY-1C provide 50-m, eight-band, and three-day observations when the images of the two sensors are combined. In this study, a DBN model is developed to fuse images from COCTS and CZI and is compared with widely used GS and IBF algorithms at the Bohai Sea. The results are analyzed at the reflectance and product levels.

The results demonstrate the following.
1) DBN can fuse COCTS and CZI multispectral images and avoid the color deviation and spectral distortion of GS and the block effect of IBF.
2) DBN is a more accurate fusion model for COCTS and CZI data compared with GS and IBF in terms of fusing the TOA reflectance. The MRE of the DBN model is at least 50% smaller than that of GS and 20% smaller than that of IBF at bands 1–6. The average GFC increases from 0.80 (GS) and 0.94 (IBF) to 0.97 (DBN), which rises by 21.25% and 3.19%, respectively. The average SSIM increases from 0.77 (GS) and 0.91 (IBF) to 0.94, which rises by 22.08% and 3.30%, respectively.
3) Images at the reflectance level rather than at the product level are recommended to fuse. The chl-a derived from the DBN-fused reflectance image obtains a higher R^2 of 0.78 and a lower RMSE of 0.10 mg/m^3 compared with the chl-a fused from GOCI and COCTS chl-a products ($R^2 = 0.56$ and RMSE $= 0.15$ mg/m^3).

Onboard the same satellite (HY-1C), COCTS and CZI sensors have the advantages of short imaging temporal gaps and high similarity of atmospheric conditions, whereas most ocean color remote sensing sensors are carried on different satellites. Thus, they provide a great opportunity to fuse the images from the two sensors and obtain suitable observations for dynamic coastal waters. The proposed DBN model can serve as a baseline for the fusion of COCTS and CZI images and a complement to the remote sensing monitoring of coastal regions. Future experiments in various waters should be performed.

ACKNOWLEDGMENT

REFERENCES

[1] C. B. Mouw *et al.*, "Aquatic color radiometry remote sensing of coastal and inland waters: Challenges and recommendations for future satellite missions," *Remote Sens. Environ.*, vol. 160, pp. 15–30, Apr. 2015.

[2] J. D. Eurico and R. L. Miller, "Bio-optical properties of coastal waters," in *Remote Sensing of Coastal Aquatic Environments: Technologies, Techniques and Applications*, R. L. Miller, C. E. D. Castillo, and B. A. McKee, Eds. Berlin, Germany: Springer, 2007, pp. 129–155.

[3] H. Loisel, V. Vantrepotte, C. Jamet, and D. N. Dat, "Challenges and new advances in ocean color remote sensing of coastal waters," in *Topics in Oceanography*, E. Zambianchi, Ed. London, U.K.: IntechOpen, 2013, pp. 89–126.

[4] S. Nayak, "Coastal zone management in India—Present status and future needs," *Geo-Spatial Inf. Sci.*, vol. 20, no. 2, pp. 174–183, 2017.

[5] J. D. Allan *et al.*, "Joint analysis of stressors and ecosystem services to enhance restoration effectiveness," *Proc. Nat. Acad. Sci.*, vol. 110, no. 1, pp. 372–377, 2013.

[6] B. S. Halpern *et al.*, "A global map of human impact on marine ecosystems," *Science*, vol. 319, no. 5865, pp. 948–952, 2008.

[7] Q. Yuan *et al.*, "Deep learning in environmental remote sensing: Achievements and challenges," *Remote Sens. Environ.*, vol. 241, May 2020, Art. no. 111716.

[8] "MODIS overview," 2020. [Online]. Available: https://lpdaac.usgs.gov/data/get-started-data/collection-overview/missions/modis-overview/

[9] "Landsat missions," United States Geol. Surv., Reston, VA, USA, 2020. [Online]. Available: https://www.usgs.gov/land-resources/nli/landsat/landsat-8?qt-science_support_page_related_con = 0#qt-science_support_page_related_con

[10] GF-4, China Center Resour. Satell. Data Appl., 2020. [Online]. Available: http://www.cresda.com/CN/Satellite/9855.shtml

[11] "HY series satellites," Nat. Satell. Ocean Appl. Service, 2020. [Online]. Available: http://www.nsoas.org.cn/news/content/2018-11/23/44_696.html

[12] C. Pohl and J. L. V. Genderen, "Review article multisensor image fusion in remote sensing: Concepts, methods and applications," *Int. J. Remote Sens.*, vol. 19, no. 5, pp. 823–854, Jan. 1998.

[13] H. Yésou, Y. Besnus, and J. Rolet, "Extraction of spectral information from Landsat TM data and merger with SPOT panchromatic imagery—A contribution to the study of geological structures," *ISPRS J. Photogramm. Remote Sens.*, vol. 48, no. 5, pp. 23–36, 1993.

[14] M. Ehlers, "Multisensor image fusion techniques in remote sensing," *ISPRS J. Photogramm. Remote Sens.*, vol. 46, no. 1, pp. 19–30, 1991.

[15] T.-M. Tu, S.-C. Su, H.-C. Shyu, and P. S. Huang, "A new look at IHS-like image fusion methods," *Inf. Fusion*, vol. 2, no. 3, pp. 177–186, Sep. 2001.

[16] X. Otazu, M. Gonzalez-Audicana, O. Fors, and J. Nunez, "Introduction of sensor spectral response into image fusion methods: Application to wavelet-based methods," *IEEE Trans. Geosci. Remote Sens.*, vol. 43, no. 10, pp. 2376–2385, Oct. 2005.

[17] C. A. Laben and B. V. Brower, "Process for enhancing the spatial resolution of multispectral imagery using pan-sharpening," US Patent 6 011 875 A, 2000.

[18] Y. Du, X. Zhang, Z. Mao, and J. Chen, "Performances of conventional fusion methods evaluated for inland water body observation using GF-1 image," *Acta Oceanol. Sinica*, vol. 38, no. 1, pp. 172–179, 2019.

[19] A. C. C. C. Silva, E. F. F. Silva, V. P. Curtarelli, L. A. S. de Carvalho, and T. S. Körting, "An evaluation of image fusion applied to inland and coastal waters," in *Proc. 19th Brazilian Symp. Remote Sens.*, 2019, vol. 19.

[20] S. Ashraf, L. Brabyn, and B. J. Hicks, "Image data fusion for the remote sensing of freshwater environments," *Appl. Geogr.*, vol. 32, no. 2, pp. 619–628, 2012.

[21] A. Minghelli-Roman, L. Polidori, S. Mathieu-Blanc, L. Loubersac, and F. Cauneau, "Spatial resolution improvement by merging MERIS–ETM images for coastal water monitoring," *IEEE Geosci. Remote Sens. Lett.*, vol. 3, no. 2, pp. 227–231, Apr. 2006.

[22] B. Zhukov, D. Oertel, F. Lanzl, and G. Reinhackel, "Unmixing-based multisensor multiresolution image fusion," *IEEE Trans. Geosci. Remote Sens.*, vol. 37, no. 3, pp. 1212–1226, May 1999.

[23] Y. Guo *et al.*, "An inversion-based fusion method for inland water remote monitoring," *IEEE J. Sel. Topics Appl. Earth Observ. Remote Sens.*, vol. 9, no. 12, pp. 5599–5611, Dec. 2016.

[24] Y. LeCun, Y. Bengio, and G. Hinton, "Deep learning," *Nature*, vol. 521, no. 7553, pp. 436–444, May 2015.

[25] C. Liu *et al.*, "Band-independent encoder–decoder network for pan-sharpening of remote sensing images," *IEEE Trans. Geosci. Remote Sens.*, vol. 58, no. 7, pp. 5208–5223, Jul. 2020.

[26] W. Xiong, Z. Xiong, Y. Cui, and Y. Lv, "A discriminative distillation network for cross-source remote sensing image retrieval," *IEEE J. Sel. Topics Appl. Earth Observ. Remote Sens.*, vol. 13, pp. 1234–1247, Mar. 2020.

[27] Y. Yu, Z. Gong, C. Wang, and P. Zhong, "An unsupervised convolutional feature fusion network for deep representation of remote sensing images," *IEEE Geosci. Remote Sens. Lett.*, vol. 15, no. 1, pp. 23–27, Jan. 2018.

[28] Y. Yu, X. Li, and F. Liu, "E-DBPN: Enhanced deep back-projection networks for remote sensing scene image superresolution," *IEEE Trans. Geosci. Remote Sens.*, vol. 58, no. 8, pp. 5503–5515, Aug. 2020.

[29] S. Zhang, Q. Yuan, J. Li, J. Sun, and X. Zhang, "Scene-adaptive remote sensing image super-resolution using a multiscale attention network," *IEEE Trans. Geosci. Remote Sens.*, vol. 58, no. 7, pp. 4764–4779, Jul. 2020.

[30] Z. Shao and J. Cai, "Remote sensing image fusion with deep convolutional neural network," *IEEE J. Sel. Topics Appl. Earth Observ. Remote Sens.*, vol. 11, no. 5, pp. 1656–1669, May 2018.

[31] Z. Shao, J. Cai, P. Fu, L. Hu, and T. Liu, "Deep learning-based fusion of Landsat-8 and Sentinel-2 images for a harmonized surface reflectance product," *Remote Sens. Environ.*, vol. 235, 2019, Art. no. 111425.

[32] H. Shen, M. Jiang, J. Li, Q. Yuan, Y. Wei, and L. Zhang, "Spatial–spectral fusion by combining deep learning and variational model," *IEEE Trans. Geosci. Remote Sens.*, vol. 57, no. 8, pp. 6169–6181, Aug. 2019.

[33] M. Ghassemi, H. Ghassemian, and M. Imani, "Deep belief networks for feature fusion in hyperspectral image classification," in *Proc. IEEE Int. Conf. Aerosp. Electron. Remote Sens. Technol.*, 2018, pp. 1–6.

[34] A. Mughees, A. Ali, and L. Tao, "Hyperspectral image classification via shape-adaptive deep learning," in *Proc. IEEE Int. Conf. Image Process.*, 2017, pp. 375–379.

[35] P. Zhong, Z. Gong, S. Li, and C.-B. Schönlieb, "Learning to diversify deep belief networks for hyperspectral image classification," *IEEE Trans. Geosci. Remote Sens.*, vol. 55, no. 6, pp. 3516–3530, Jun. 2017.

[36] Z. Gong, P. Zhong, J. Shan, and W. Hu, "A diversified deep ensemble for hyperspectral image classification," in *Proc. 9th Workshop Hyperspectral Image Signal Process., Evol. Remote Sens.*, 2018, pp. 1–5.

[37] W. Diao, X. Sun, X. Zheng, F. Dou, H. Wang, and K. Fu, "Efficient saliency-based object detection in remote sensing images using deep belief networks," *IEEE Geosci. Remote Sens. Lett.*, vol. 13, no. 2, pp. 137–141, Feb. 2016.

[38] H. Shen, T. Li, Q. Yuan, and L. Zhang, "Estimating regional ground-level $PM_{2.5}$ directly from satellite top-of-atmosphere reflectance using deep belief networks," *J. Geophys. Res. Atmos.*, vol. 123, no. 24, pp. 13875–13886, Dec. 2018.

[39] X. Chen *et al.*, "Coupling remote sensing retrieval with numerical simulation for SPM study—Taking Bohai sea in China as a case," *Int. J. Appl. Earth Observ. Geoinf.*, vol. 12, pp. S203–S211, Sep. 2010.

[40] C. Chen, H. Liu, and R. C. Beardsley, "An unstructured grid, finite-volume, three-dimensional, primitive equations ocean model: Application to coastal ocean and estuaries," *J. Atmos. Ocean. Technol.*, vol. 20, no. 1, pp. 159–186, Jan. 2003.

[41] M.-E. Ren and Y.-L. Shi, "Sediment discharge of the Yellow river (China) and its effect on the sedimentation of the Bohai and the Yellow sea," *Continental Shelf Res.*, vol. 6, no. 6, pp. 785–810, Jan. 1986.

[42] A. Suo, Y. Lin, and M. Zhang, "Regional difference of coastal land use around the Bohai sea based on remote sensing images," *Multimedia Tools Appl.*, vol. 75, no. 19, pp. 12061–12075, Oct. 2016.

[43] D. Sun, Y. Huan, Z. Qiu, C. Hu, S. Wang, and Y. He, "Remote-sensing estimation of phytoplankton size classes from GOCI satellite measurements in Bohai sea and Yellow sea," *J. Geophys. Res. Oceans*, vol. 122, no. 10, pp. 8309–8325, Oct. 2017.

[44] Nat. Bur. Statist. China, "Transport, post and telecommunication services," in *China Statistical Yearbook 2013*, M. Jiantang, Ed. Beijing, China: China Statist. Press, 2013.

[45] Fisheries Bur. Ministry Agriculture China, "Production factors," in *Chinese Fishery Statistical Yearbook 2013*. Beijing, China: China Agriculture Press, 2013.

[46] J. Zhang *et al.*, "Heavy aerosol loading over the Bohai bay as revealed by ground and satellite remote sensing," *Atmos. Environ.*, vol. 124, pp. 252–261, Jan. 2016.

[47] X. Gao, F. Zhou, and C.-T. A. Chen, "Pollution status of the Bohai sea: An overview of the environmental quality assessment related trace metals," *Environ. Int.*, vol. 62, pp. 12–30, Jan. 2014.

[48] J. H. Ryu, J. K. Choi, J. Eom, and J. H. Ahn, "Temporal variation in Korean coastal waters using geostationary ocean color imager," *J. Coastal Res.*, vol. 64, pp. 1731–1735, 2011.

[49] J.-K. Choi, Y. J. Park, J. H. Ahn, H.-S. Lim, J. Eom, and J.-H. Ryu, "GOCI, the world's first geostationary ocean color observation satellite, for the monitoring of temporal variability in coastal water turbidity," *J. Geophys. Res. Oceans*, vol. 117, no. C9, Sep. 2012.

[50] J.-E. Yoon *et al.*, "Assessment of satellite-based chlorophyll-a algorithms in eutrophic Korean coastal waters: Jinhae bay case study," (in English), *Frontiers Mar. Sci.*, vol. 6, Jun. 2019.

[51] M. Wang *et al.*, "Ocean color products from the Korean geostationary ocean color imager (GOCI)," *Opt. Express*, vol. 21, no. 3, pp. 3835–3849, 2013.

[52] C. Hu, L. Feng, and Z. Lee, "Evaluation of GOCI sensitivity for At-sensor radiance and GDPS-retrieved chlorophyll-a products," *Ocean Sci. J.*, vol. 47, no. 3, pp. 279–285, Sep. 2012.

[53] J. Li, X. Chen, L. Tian, J. Ding, Q. Song, and Z. Yu, "On the consistency of HJ-1A CCD1 and Terra/MODIS measurements for improved spatio-temporal monitoring of inland water: A case in Poyang lake," *Remote Sens. Lett.*, vol. 6, no. 5, pp. 351–359, 2015.

[54] G. Schaepman-Strub, T. Painter, S. Huber, S. Dangel, M. E. Schaepman, and F. Berendse, "About the importance of the definition of reflectance quantities-results of case studies," in *Proc. Int. Arch. Photogramm., Remote Sens. Spatial Inf. Sci.*, Istanbul, Turkey, 2004, pp. 361–366.

[55] J. Li, X. Chen, L. Tian, J. Huang, and L. Feng, "Improved capabilities of the Chinese high-resolution remote sensing satellite GF-1 for monitoring suspended particulate matter (SPM) in inland waters: Radiometric and spatial considerations," *ISPRS J. Photogramm. Remote Sens.*, vol. 106, pp. 145–156, 2015.

[56] D. E. Rumelhart, G. E. Hinton, and R. J. Williams, "Learning representations by back-propagating errors," *Nature*, vol. 323, no. 6088, pp. 533–536, Oct. 1986.

[57] R. Dian, S. Li, A. Guo, and L. Fang, "Deep hyperspectral image sharpening," *IEEE Trans. Neural Netw. Learn. Syst.*, vol. 29, no. 11, pp. 5345–5355, Nov. 2018.

[58] Z. Wang, A. C. Bovik, H. R. Sheikh, and E. P. Simoncelli, "Image quality assessment: From error visibility to structural similarity," *IEEE Trans. Image Process.*, vol. 13, no. 4, pp. 600–612, Apr. 2004.

[59] R. M. H. Nguyen, D. K. Prasad, and M. S. Brown, "Training-based spectral reconstruction from a single RGB image," in *Computer Vision–ECCV 2014*. New York, NY, USA: Springer, 2014, pp. 186–201.

[60] K. Shi *et al.*, "Remote chlorophyll-a estimates for inland waters based on a cluster-based classification," *Sci. Total Environ.*, vol. 444, pp. 1–15, 2013.

[61] R. P. Bukata, J. H. Jerome, K. Y. Kondratyev, A. S. Kondratyev, and D. V. Pozdnyakov, *Optical Properties and Remote Sensing of Inland and Coastal Waters*. Boca Raton, FL, USA: CRC Press, 1995.

[62] Y. Sakuno, "Accuracy evaluation of chlorophyll product data of geostationaly ocean color satellite, "GOCI" in inner bay," *J. Jpn. Soc. Civil Eng., B3 (Ocean Eng.)*, vol. 68, no. 2, pp. I582–I587, 2012.

[63] J.-E. Moon, Y.-H. Ahn, J.-H. Ryu, and P. Shanmugam, "Development of ocean environmental algorithms for geostationary ocean color imager (GOCI)," *Korean J. Remote Sens.*, vol. 26, no. 2, pp. 163–168, 2010.

[64] S. W. Bailey, B. A. Franz, and P. J. Werdell, "Estimation of near-infrared water-leaving reflectance for satellite ocean color data processing," *Opt. Express*, vol. 18, no. 7, pp. 7521–7527, 2010.

[65] N.-B. Chang, B. Vannah, and Y. J. Yang, "Comparative sensor fusion between hyperspectral and multispectral satellite sensors for monitoring microcystin distribution in lake erie," *IEEE J. Sel. Topics Appl. Earth Observ. Remote Sens.*, vol. 7, no. 6, pp. 2426–2442, Jun. 2014.

[66] C. Doña *et al.*, "Integrated satellite data fusion and mining for monitoring lake water quality status of the Albufera de Valencia in Spain," *J. Environ. Manage.*, vol. 151, pp. 416–426, 2015.

[67] Y. Pan, F. Shen, and X. Wei, "Fusion of Landsat-8/OLI and GOCI data for hourly mapping of suspended particulate matter at high spatial resolution: A case study in the Yangtze (Changjiang) estuary," *Remote Sens.*, vol. 10, no. 2, 2018.

Hongren Ji received the B.E. degree in surveying and mapping engineering from Central South University, Changsha, China, in 2018. He is currently working toward the master's degree in photogrammetry and remote sensing with Wuhan University, Wuhan, China.

His main research interests include water color remote sensing and image fusion of satellite sensors.

Ruqing Tong received the B.E. degree in surveying and mapping engineering, in 2020 from Wuhan University, Wuhan, China, where she is currently working toward the master's degree in photogrammetry and remote sensing.

Her main research interest include water color remote sensing.

Liqiao Tian received the Ph.D. degree in geography and geographic information systems from Wuhan University, Wuhan, China, in 2008.

Since July 2008, he has been with the State Key Laboratory of Information Engineering in Surveying, Mapping, and Remote Sensing, Wuhan University. His current research interest includes application of remote sensing.
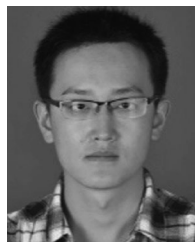
Yulong Guo received the Ph.D. degree in remote sensing application from Nanjing Normal University, Nanjing, China, in 2015.

He is currently at Henan Agricultural University, Zhengzhou, China. His research interests include water color remote sensing and image fusion.
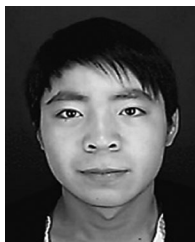
Jian Li received the Ph.D. degree in remote sensing from Wuhan University, Wuhan, China, in 2015.

He is currently a Postdoctor with the School of Remote Sensing and Information Engineering, Wuhan University. His main research interests include lake and coastal environment remote sensing and assessment.

Qun Zeng received the Ph.D. degree in physical geography from East China Normal University, Shanghai, China, in 2005.

Since 2006, she has been with the Editorial Department of Journal, Central China Normal University, Wuhan, China. Her current research interest include the application of remote sensing and GIS in physical geography.